Geophysical Research Letters®

RESEARCH LETTER
10.1029/2021GL093982

Evolution of the Horizontal Winds in Jupiter's Great Red Spot From One Jovian Year of HST/WFC3 Maps

Michael H. Wong[1], Philip S. Marcus[1], Amy A. Simon[2], Imke de Pater[1], Joshua W. Tollefson[1], and Xylar Asay-Davis[3]

[1]Center for Integrative Planetary Science, University of California, Berkeley, CA, USA, [2]Solar System Exploration Division, NASA Goddard Space Flight Center, Greenbelt, MD, USA, [3]Los Alamos National Laboratory, Los Alamos, NM, USA

Key Points:

- A high-speed ring marking the edge of the Great Red Spot velocity field has been shrinking and circularizing at a roughly constant rate
- Mean wind speeds within the high-speed ring have increased by 4%–8% from 2009 to 2020, at a roughly constant rate
- Velocity field changes coincided with a major 2016 storm, but we found no changes in 2019 when red material flaked away from the main oval

Supporting Information:

Supporting Information may be found in the online version of this article.

Correspondence to:

M. H. Wong,
mikewong@astro.berkeley.edu

Citation:

Wong, M. H., Marcus, P. S., Simon, A. A., de Pater, I., Tollefson, J. W., & Asay-Davis, X. (2021). Evolution of the horizontal winds in Jupiter's Great Red Spot from one Jovian year of HST/WFC3 maps. *Geophysical Research Letters*, *48*, e2021GL093982. https://doi.org/10.1029/2021GL093982

Received 22 APR 2021
Accepted 20 AUG 2021

Abstract We measured the horizontal winds in Jupiter's Great Red Spot (GRS) using data from the WFC3/UVIS instrument on board the Hubble Space Telescope (HST). The data cover 11 epochs from 2009 to 2020. Long-term monotonic trends in size and shape previously noted from the visible cloud appearance are paralleled by changes in the high-speed ring around the vortex. The circularization of the GRS cannot be explained by changes in the horizontal wind shear of the surrounding environment. The velocity fields suggest no long-term trend in the static stability inside or outside the vortex. Instead, the changes are accompanied by a 4%–8% increase in the mean wind speeds of the high-speed ring from 2009 to 2020. Changes in the wind field coincided with the South Equatorial Belt Outbreak storms of 2016–2017, but not with 2019 "flaking" events involving detachment of red material from the main oval.

Plain Language Summary We measured the horizontal winds in Jupiter's Great Red Spot (GRS) using data from the WFC3/UVIS instrument on board the Hubble Space Telescope (HST). The data cover 11 time periods from 2009 to 2020. Winds blow fastest in a high-speed ring around the outside of the GRS. Previous pictures of the clouds showed that the GRS was shrinking and becoming more like a circle and less like an oval. We measure similar changes in the high-speed ring. We rule out some possible causes for the changes: changes in the wind shear of the surrounding atmosphere, or changes in how temperature varies with height. As the GRS shrinks and circularizes, the average wind speed in the high-speed ring gets faster. Some changes in the GRS wind patterns happened at the same time as a giant nearby storm in 2016/2017, but we did not find changes at the same time as flaking events in 2019. By "flaking" we mean pictures showing that small areas of red, normally kept inside the GRS, detached and blew away from the spot.

1. Introduction

The Great Red Spot is an enduring large anticyclone in Jupiter's atmosphere, situated in the South Tropical Zone (Figure 1). Anticyclonic flow in this zone is perturbed over the northern edge of the GRS so that it locally protrudes into the typically dark and reddish South Equatorial Belt (SEB) to the north. The SEB features dramatic global-scale changes in coloration, cloud properties, and convective activity (e.g., Fletcher et al., 2011, 2017; Rogers, 1995; Sánchez-Lavega & Gómez, 1996), but the most notable change in the GRS itself is more monotonic in nature: a continuous decrease in size over more than 100 years of accurate observations (Simon et al., 2018).

The size and longevity of the GRS make it unique among outer solar system vortices, yet it also serves as an archetype of a class of "pancake vortices"—anticyclones embedded in stably stratified fluids—also including vortices like the dark spots on Neptune and salt lens eddies in the Earth's oceans (e.g., Dowling, 1995; Hassanzadeh et al., 2012; Yim et al., 2016). Pancake vortices have a thickness much smaller than their horizontal dimensions, like the GRS whose horizontal scale is some 50 times greater than vertical scale, according to theoretical arguments based on laboratory experiments and Jovian vortex velocity fields (Lemasquerier et al., 2020). Terrestrial ocean eddies transport heat meridionally by both stirring (turbulent) and trapping (bulk transport) mechanisms (Sun et al., 2018). Trapping is limited on Jupiter because major vortices are bounded by jets that limit meridional migration, although trapping could be significant on Saturn, where poleward migration of the anticyclone created by the 2010 Great White Storm was observed

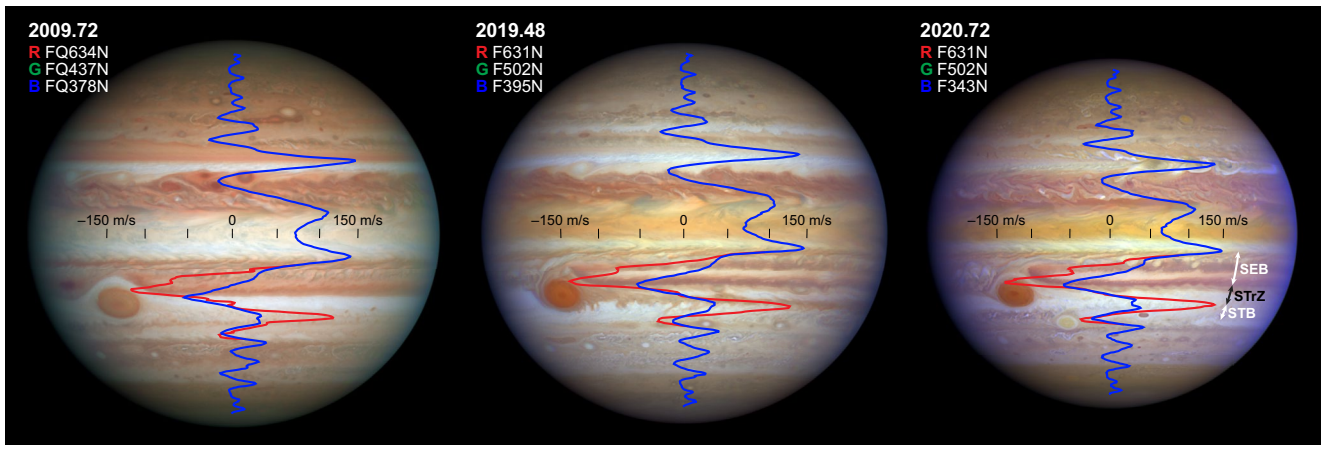

Figure 1. Jupiter data spanning one Jupiter year of HST/WFC3 observations, with zonal (blue) and Great Red Spot east-west (red) wind profiles overlaid. Arrows at right mark the latitude ranges of the South Equatorial Belt (SEB), South Tropical Zone (STrZ), and South Temperate Belt (STB). Color contrast has been maximized. Some subtle remaining color differences are due to different filter sets available at each epoch.

(Hueso et al., 2020; Sayanagi et al., 2013). Marcus (2004) suggested that the stirring mechanism—driven by the chaotic behavior of Jupiter's three white ovals near 34°S—would change after the ovals merged in 1997–2000, possibly leading to a temperature change at that latitude. The color change of merged Oval BA in 2006 might have resulted from a temperature change (e.g., de Pater et al., 2010; Wong et al., 2011), but the evidence is inconclusive in light of later changes in Oval BA back to white coloration (Simon, 2015), plus the general lack of high-resolution photometric time-series color information covering the white ovals in the decades prior to their mergers. Studying vortex evolution over time may allow comparison between planetary fluid environments from the atmospheres of the giant planets to the terrestrial oceans.

2. Data and Methodology

Data were acquired by HST/WFC3 (Dressel, 2021) over the 2009–2020 time period by programs listed in Table S2. Additional 2014 data were not included because satellite-shadowing of the GRS region prevented high-precision velocity fields from being derived (Simon et al., 2014). Red wavelength (631–763 nm) filters optimize both spatial resolution and cloud tracer contrast. These "continuum" filters are sensitive to cloud opacity throughout the $P < 10$ bar region, but most of the clouds trace velocities at $P < 1$ bar in the GRS (Banfield et al., 1998). Image processing consisted of correction for cosmic rays and detector distortion, and transformation from sky coordinates to Jovian latitude/longitude coordinates. We use planetographic latitudes and System III longitudes (Wong et al., 2020).

We retrieve the velocity field using the Advection Corrected Correlation Image Velocimetry (ACCIV) technique, which was specifically developed to measure velocities along curved paths in Jupiter's anticyclones (Asay-Davis et al., 2009; Asay-Davis, 2015). In a two-pass approach, we use data with a typical time separation of 1.6 h for the initial pass, and 10.8 h for the final pass. At each iterative step, the velocity field from the previous iteration is used to advect the images to a common time point, and correlations are found between these advected images to refine the velocity field and to characterize the final uncertainties. We estimate an average "correlation velocity uncertainty" (Asay-Davis et al., 2009) of 3.6 ± 1.2 m s^{-1} among all the velocity fields (Table S4). The final output of ACCIV consists of one velocity field data set with the full set of scattered velocity vectors, and one sampled on a regular grid. Velocity fields and related data files are available in a public archive (Wong, 2021). The Supporting Information S1 discusses the error budget for uncertainty estimation, the archived data, and the ACCIV control parameters.

The overall dynamical structure of the GRS is defined by a ring of high-speed winds, which we use as a definition of the vortex dynamical boundary (even though the area just outside the high-speed ring is also part of the vortex; see Figure S3). Two alternate methods characterize the velocities in this ring:

1. We used an automated process to fit a symmetric ellipse to the data (see Supporting Information S1), thereby defining the vortex center location. Within the symmetric ellipse, we measured azimuthal velocities $v_{ellipse}$.
2. We defined a series of 100 "spokes" radiating from the center of the GRS with equal angular spacing, measuring the maximum azimuthal velocity v_{spokes} along each spoke. The path connecting maxima along each spoke defines a lumpy ring, deviating from a perfect ellipse (Figure S2).

Figure 2 shows the 2020.72 velocity field, including the symmetric ellipse fit to the high-speed ring, gridded and scattered-vector velocity fields, the relative vorticity map, and cuts through the principal axes of the vortex. The global-average zonal wind field was subtracted to emphasize features of the velocity field specific to the vortex (except in Figure 2f).

3. Results

The relative vorticity map of the GRS, and the size and shape of the high-speed ring, are shown for each epoch in Figure 3. An outer region with a hollow core (Figure S3) can be seen at every epoch. The mean absolute value of the relative vorticity in the outer region remained in the 4×10^{-5} to 5×10^{-5} s^{-1} range throughout the timeline. Both the morphology and the unchanging constant relative vorticity are consistent with the study of Shetty and Marcus (2010), which found constant potential vorticity (a different quantity) within uncertainties, using a model of GRS velocity fields spanning 1979–2006. Constant relative vorticity implies constant potential vorticity only if static stability does not change over time, which we demonstrate below in the discussion of Figure 4c. Static stability can be expressed in terms of the Brunt-Väisälä frequency, the deformation radius, or the lapse rate (e.g., Equation 1 of Wong et al., 2011).

Changes in the size of the vortex (Figure 4a and Table 1) extend the trends described in Simon et al. (2014, 2018). Extrapolating the linear decrease in size leads to an estimate that the GRS will reach a circular shape in 2035 based on HST/WFC3 data alone, or in 2039 if data extending back to Voyager are included.

Figure 4b shows that the mean wind speeds in the high-speed ring have increased over time. Weighted least squares fits give a rate of increase of 0.69 ± 0.25 m s^{-1} yr^{-1} using $v_{ellipse}$ or 0.38 ± 0.25 m s^{-1} yr^{-1} using v_{spokes}. Two separate statistical tests show that the increase is significant:

1. The Pearson's r values (Press et al., 1992, p.636), which are independent of measurement uncertainty, are $r = 0.674$ (with a false-alarm probability for linear correlation of 3.5%) for $v_{ellipse}$, and $r = 0.579$ (with a false-alarm probability for linear correlation of 8.2%) for v_{spokes}.
2. Reduced χ_ν^2 values (which depend on measurement uncertainties) are 0.79 (for $v_{ellipse}$) or 0.77 (for v_{spokes}), with $\chi_\nu^2 > 0.5$ indicating that a linear slope is a good model for the variation (Bevington & Robinson, 1992, p.197).

The spatial variability in values of $v_{ellipse}$ or v_{spokes} measured around the GRS circumference for a typical velocity field is shown by the shaded bars on the left side of Figure 4b, with magnitudes on the order of ± 15 m s^{-1}. The variability in velocities (also visible as lumps in the red ring in Figure 2b) is probably a real characteristic of the velocity field, rather than a result of errors in the retrieval process. We calculate χ_ν^2 for the linear trend in Figure 4b, using the variability around the ring at each epoch (shaded bars) as an estimate of the mean speed uncertainty, rather than the error bars shown at each point based on the "correlation velocity uncertainty" described in Asay-Davis et al. (2009). The resulting χ_ν^2 of 0.04 is unreasonably small, meaning that if the variability around the ring were truly due to measurement uncertainty (noise), then it is highly improbable that the data points would adhere so closely to the fitted lines shown.

Characteristics of the GRS flow field that are sensitive to the static stability (i.e., the vertical temperature profile) inside and outside of the vortex did not show strong trends (Figure 4c). To quantitatively constrain changes in the static stability (although we do not directly measure the static stability itself), we follow the work of Shetty et al. (2007), which found that the shape of east-west and north-south velocity profiles through the vortex center were sensitive to the potential vorticity. Potential vorticity is a nonlinear function of both the relative vorticity (velocity field gradient) and the static stability (expressed

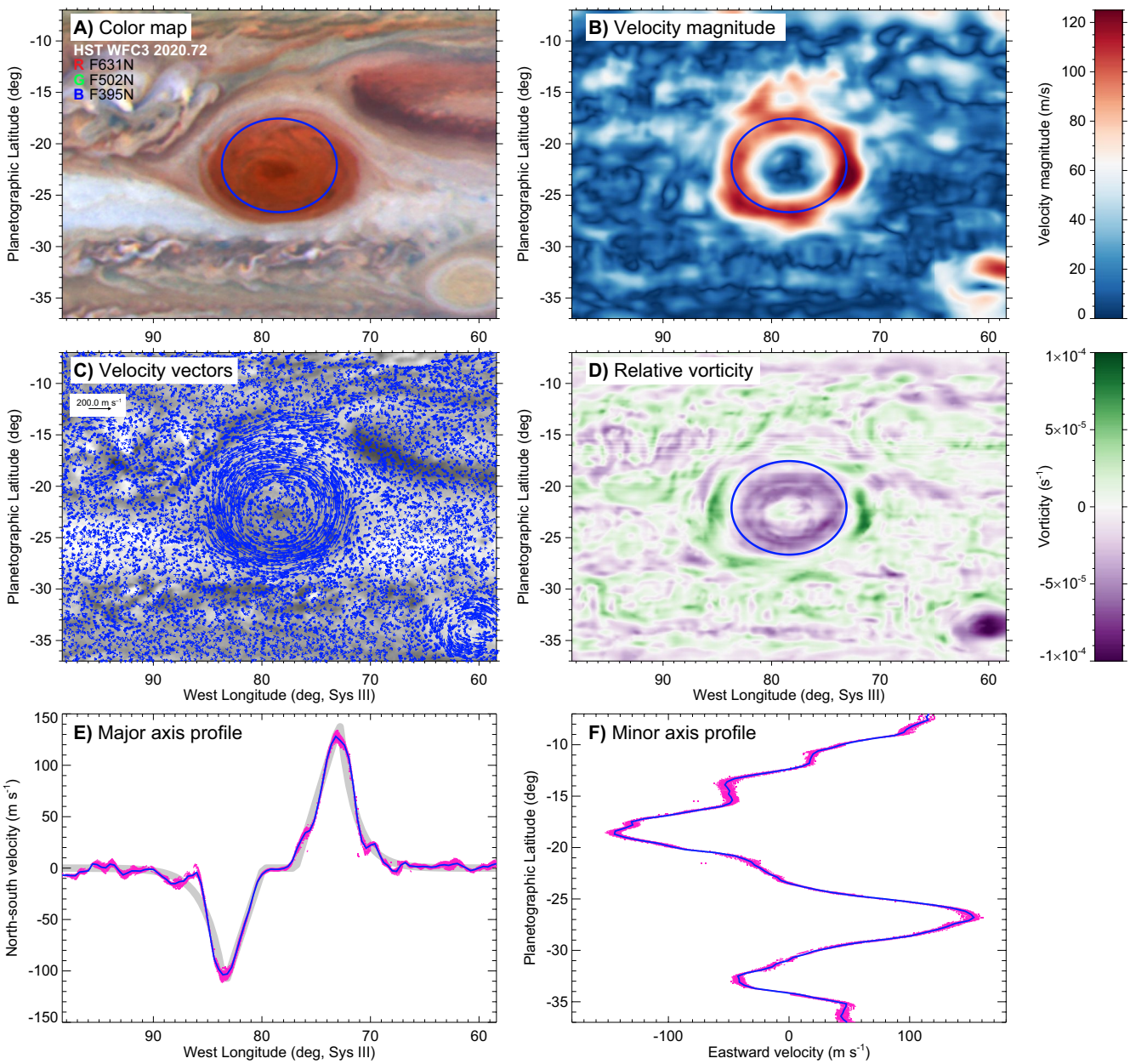

Figure 2. Great Red Spot velocity field data for the 2020.72 epoch, which is based on data from the OPAL program (Simon et al., 2015). The mean zonal wind field has been subtracted from the 2D velocity fields. (a) Color composite map, with a blue ring indicating the best-fit symmetric ellipse of high-speed winds. (b) Wind speed, after subtraction of the mean zonal wind profile. (c) Velocity vectors (10^4 vectors drawn from the full set of 5.9×10^6 vectors). (d) Relative vorticity, showing the "hollow" core. (e) Northward velocities along an east-west profile through the center of the ellipse. Individual north-south vector components within ±0.25° of the east-west line are shown in light red, with the mean profile shown in blue. A parameterized fit to the profile is shown in light grey. (f) As panel E, for eastward velocities along a north-south profile through the center.

as the deformation radius L_R in Shetty et al., 2007). Thus, if we could show that the relative vorticity in the GRS was unchanged, and the shape of the velocity profile across the vortex was unchanged, we could conclude that the static stability in the vortex was unchanged. Figure 4c shows fluctuations of about ±25% in the GRS relative vorticity (gold points) and the decay factors characterizing the flow inside (blue points) and outside (pink points) of the high-speed ring, which are respectively sensitive to the potential vorticity inside and outside the ring. The overall trend in the mean speed is not reflected in these data.

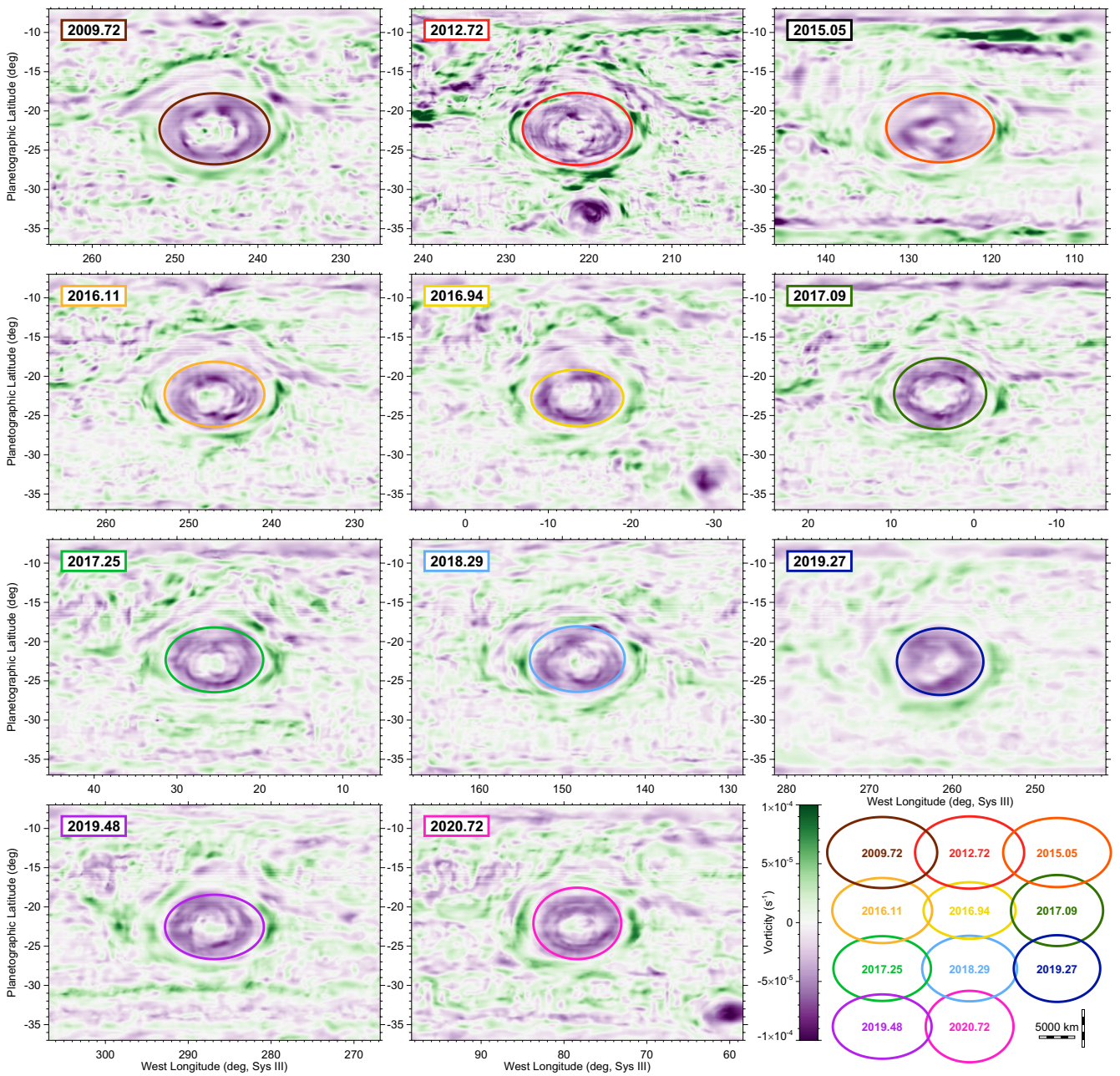

Figure 3. Relative vorticity maps (as in Figure 2d) for all epochs. At lower right, the evolution of the high-speed ring over the 2009–2020 period (shown at the same horizontal scale as the map panels) includes changes in shape and size on both short and long timescales.

To rule out the possibility that changes in the GRS velocity field were due to changes in the vortex surroundings, we measured the mean wind shear (applying a linear fit to the zonal wind profile) over the 20–25°S range (Figure 4d). Methodology for the zonal wind retrievals is described in Asay-Davis et al. (2011) and Tollefson et al. (2017). There is no monotonic change in the wind shear (with the 2009 data point included) that parallels the long-term trends in vortex size, shape, and average wind velocity in the high-speed ring. We also found that the Rossby number of the GRS did not follow the long-term trends. The non-dimensional Rossby number $Ro = U/fL$ characterizes the relative strength of inertial and Coriolis forces, where U is the horizontal velocity scale, f is the Coriolis parameter, and L is the horizontal length scale.

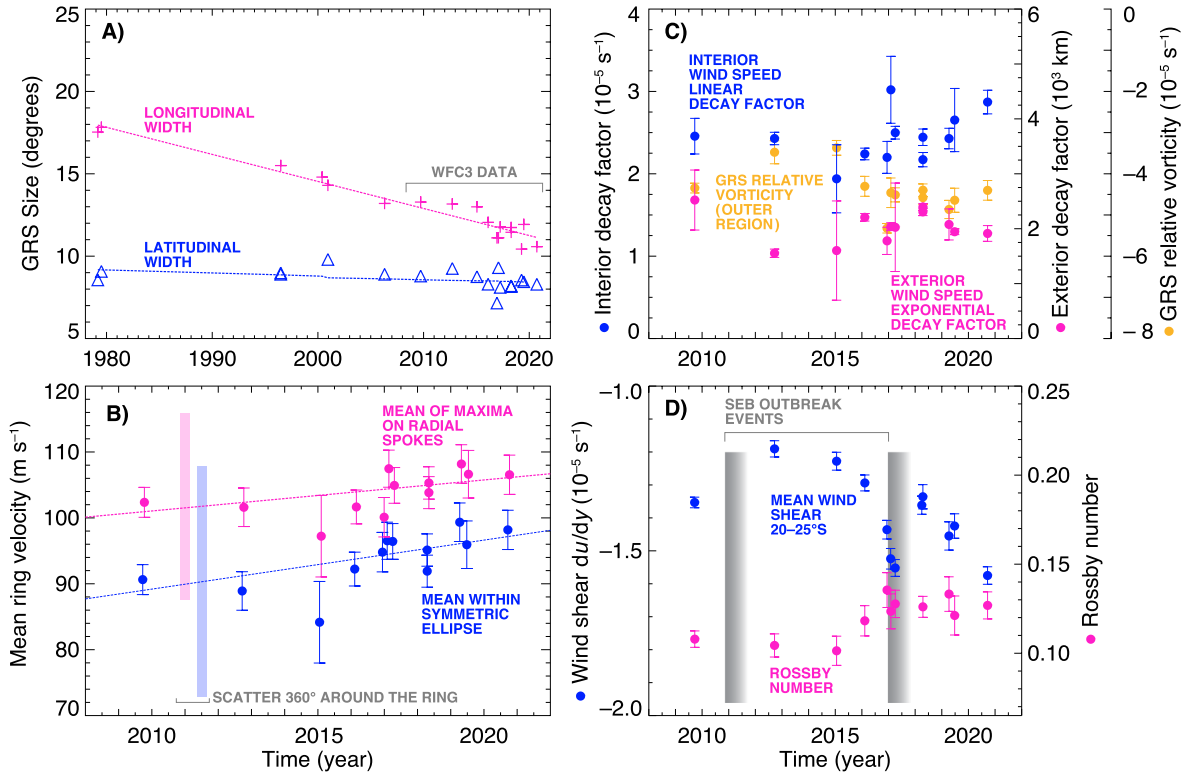

Figure 4. Evolution of the great red spot (GRS) velocity field. (a) There is a long-term decrease in size and aspect ratio of the high-speed ring, along with short-timescale variability. Data include previously published velocity fields from Voyager, Galileo, Cassini, and other HST instruments (Asay-Davis et al., 2009; Dowling & Ingersoll, 1988; Mitchell et al., 1981; Vasavada et al., 1998). (b) Two different methods measure a small but statistically significant increase in the mean wind speed in the high-speed ring of the GRS (see text). (c) Neither relative vorticity in the GRS outer region nor traits of the velocity field sensitive to atmospheric static stability showed long-term trends. Velocity field traits quantify the decay of wind speed inside (blue) and outside (pink) the high-speed ring as simple linear/exponential functions (thick gray line in Figure 2e). Data shown are averages of parameters for the east and west vertices of the GRS. (d) The STrZ windshear and the Rossby number characterizing the flow of the GRS high-speed ring both intensified around the time of the SEB Outbreak convective event in 2016/2017.

The GRS *Ro* and the SEB wind shear did feature sudden changes in the 2016–2017 time period. The Rossby number increased from 0.105 ± 0.002 prior to 2016 to 0.127 ± 0.002 in 2016 and later, while there was a transient intensification of the SEB wind shear in 2017. The increase in the GRS *Ro* means that the flow of

Table 1
Retrieved Velocity Field Parameters Pertaining to the High-Speed Ring Around the Great Red Spot

UT Date (series midpoint)	Fractional year	Major width (deg)	Major width (10^3 km)	Minor width (deg)	Minor width (10^3 km)	Aspect ratio	Mean speed $v_{ellipse}$ (m s^{-1})	Mean speed v_{spokes} (m s^{-1})
2009-09-22 16:37	2009.72	13.27 ± 0.48	15.59 ± 0.56	9.05 ± 0.48	11.21 ± 0.60	1.39 ± 0.09	92 ± 14	103 ± 12
2012-09-20 15:42	2012.72	13.17 ± 0.66	15.44 ± 0.77	9.20 ± 0.74	11.40 ± 0.91	1.35 ± 0.13	89 ± 24	102 ± 17
2015-01-19 13:53	2015.05	12.99 ± 0.92	15.23 ± 1.08	8.80 ± 0.86	10.90 ± 1.07	1.40 ± 0.17	84 ± 19	97 ± 17
2016-02-09 16:03	2016.11	12.05 ± 0.76	14.17 ± 0.89	8.30 ± 0.72	10.28 ± 0.89	1.38 ± 0.15	92 ± 13	102 ± 11
2016-12-11 19:42	2016.94	11.11 ± 0.82	13.11 ± 0.97	7.20 ± 0.49	8.93 ± 0.61	1.47 ± 0.15	95 ± 18	100 ± 14
2017-02-01 22:50	2017.09	11.12 ± 0.84	13.02 ± 0.99	9.05 ± 0.76	11.21 ± 0.94	1.16 ± 0.13	97 ± 17	107 ± 16
2017-04-03 08:08	2017.25	11.77 ± 0.70	13.88 ± 0.83	8.25 ± 0.50	10.23 ± 0.62	1.36 ± 0.12	97 ± 13	105 ± 8
2018-04-17 07:49	2018.29	11.74 ± 0.51	13.82 ± 0.59	8.20 ± 0.43	10.16 ± 0.54	1.36 ± 0.09	95 ± 17	105 ± 15
2019-04-09 18:44	2019.27	10.43 ± 0.66	12.21 ± 0.78	8.50 ± 0.71	10.52 ± 0.88	1.16 ± 0.12	100 ± 12	108 ± 11
2019-06-26 12:46	2019.48	11.93 ± 1.02	13.96 ± 1.19	8.20 ± 0.81	10.15 ± 1.01	1.37 ± 0.18	96 ± 17	107 ± 11
2020-09-20 08:15	2020.72	10.59 ± 0.49	12.41 ± 0.57	9.10 ± 0.67	11.27 ± 0.83	1.10 ± 0.10	99 ± 12	106 ± 9

the vortex became slightly less "large scale" (i.e., less sensitive to planetary rotation, Pedlosky, 1987), but the vortex remains very much in the geostrophic regime.

4. Discussion

Long-term change in the aspect ratio could be explained if there were a decrease in the magnitude of the anticyclonic shear in the surrounding flow, because shear in the environment of vortices causes departures from circular shape (e.g., Marcus, 1990; Moore & Saffman, 1971). The environmental wind shear over the 2009–2020 timeframe did not weaken. It is unclear whether the wind shear is intensifying over time (which would elongate rather than circularize the GRS in the absence of any other influences), or whether it is varying in a more complex way.

The velocity fields also rule out a long-term variation in static stability, through comparison of relative vorticity in the GRS outer region with the shape of the velocity profile across the ring (represented by "decay factors"). Shetty et al. (2007) showed that the east-west cut through the vortex center had a simpler shape compared to the north-south cut, where interactions with the zonal jet also affect the velocity profiles. Although Galileo Probe measurements and theoretical analyses suggest static stability varies with height (Magalhães et al., 2002; Sugiyama et al., 2006; Wong, 2009), quasi-geostrophic models such as Shetty et al. (2007) treat it as vertically uniform. Likewise, retrieved horizontal wind fields only apply to a limited altitude range compared to the full vertical extent of the vortex. Subject to these types of limitations, vortex models constrained by imaging and wind field data have been extensively used to estimate atmospheric static stability on Jupiter, with many finding a deformation radius of about 2,000 km (e.g., Brueshaber & Sayanagi, 2021; Brueshaber et al., 2019; Cho et al., 2001; Shetty & Marcus, 2010).

Wind speeds vary azimuthally by about ± 15 m s^{-1} around the circumference of the high-speed ring. This variability includes a time-dependent component, as suggested by Choi et al. (2007) to explain trajectory curves that did not converge in their velocity field analysis of Galileo imager data. Velocity fields from spacecraft and HST observations of Jovian vortices also varied as a function of azimuthal position angle, with effects seen in the derived relative vorticity maps and profiles (e.g., Choi et al., 2010; Mitchell et al., 1981; Sánchez-Lavega et al., 2021). These variations could result from perturbations within the high-speed ring such as Rossby waves (Choi et al., 2007).

Evolutionary processes in terrestrial ocean eddies may help explain the changes in the GRS, despite key differences between Jovian and terrestrial vortices such as compressibility. Measurements of the evolution of a "meddy" in the Atlantic Ocean between 1984 and 1985 showed a decrease in size accompanied by a slight increase in rotation rate (Schultz Tokos & Rossby, 1991), which may be explained by a redistribution of angular momentum after erosion of the vortex core (Sutyrin, 2020). "Flaking" events in mid-2019 (Sánchez-Lavega et al., 2021), in which regions of red material were seen to detach from the GRS and persist outside the oval itself for some time, were not associated with significant deviation from the long term evolutionary trends. So even if long term trends (in vortex size, shape, and peak windspeeds) are attributed to vortex erosion, we agree with the findings of Sánchez-Lavega et al. (2021) that the flakes did not represent an increase in erosive activity.

Although we lack theoretical insight into the cause of significant velocity field changes seen in 2016, it is notable that a major convective event at nearby latitudes—the South Equatorial Belt Outbreak (SEBO)— began in December 2016 and persisted into 2017 (Rogers, 2018; de Pater et al., 2019). The GRS Rossby number had already begun to increase in February 2016, indicating a several-month development timescale prior to the outbreak of convective activity on 29 December 2016. A previous SEBO event occurred in November 2010 (Fletcher et al., 2017), but there were no velocity field data to determine if that event also affected the global wind shear over 20–25°S or the GRS *Ro*.

On the other hand, the GRS velocity field seems to be insensitive to an interaction with a large triangular South Tropical Disturbance (STrD) phenomenon in 2017–2018. The STrD originated near a large cyclonic vortex (Rogers et al., 2018), supporting ideas that STrDs are visible manifestations of stagnation points in the interacting flow field of jets and vortices (Marcus et al., 2008). Features like the 2019 GRS flakes also were produced near stagnation points (Marcus et al., 2019). Perhaps stagnation point interactions are able

to produce conspicuous changes in cloud appearance, but do not perturb a large span of pressure levels (i.e., by changing the stratification) and thus do not affect properties like the GRS *Ro* and the zonal wind shear.

Vortex oscillations—in both shape and location—were seen in Voyager Neptune imaging (Smith et al., 1989; Sromovsky et al., 1993, 2002), and oscillations provide a major constraint for dynamical models (LeBeau & Dowling, 1998; Hadland et al., 2020; Polvani et al., 1990). A triple-vortex system on Saturn oscillated in longitude (del Río-Gaztelurrutia et al., 2018), although long-lived single Saturnian vortices did not oscillate in Voyager observations (Sánchez-Lavega et al., 2000). The GRS has a well-known 90-day oscillation in longitudinal position (Trigo-Rodriguez et al., 2000), which was perturbed during the flaking events of 2019 (Sánchez-Lavega et al., 2021). Short timescale variations in the GRS size/shape (Figure 3, Table 1) could be due to periodic oscillations or transient changes, but future high-cadence datasets are needed to compare this dynamical aspect of anticyclones in outer planet atmospheres.

Data Availability Statement

All data from this project are available from a science-product repository at the MAST archive (Wong 2021).

Acknowledgments
The analysis is based on observations from programs listed in Table S2, made with WFC3 on the NASA/ESA HST, obtained at the Space Telescope Science Institute (STScI), which is operated by AURA under NASA contract NAS 5-26555, with support from all programs listed except 13067, and additional support from program 13631. We are grateful for the STScI approval to repeat failed 2020 observations for program 15929, without which GRS velocities would have been impossible to measure. We appreciate high-quality review comments from two anonymous reviewers, which caused a factor of three expansion of the Supporting Information S1 document.

References

Asay-Davis, X. S. (2015). Corrected Correlation Image Velocimetry (ACCIV). GitHub Code Repository. https://github.com/xylar/acciv

Asay-Davis, X. S., Marcus, P. S., Wong, M. H., & de Pater, I. (2009). Jupiter's shrinking Great Red Spot and steady Oval BA: Velocity measurements with the 'Advection Corrected Correlation Image Velocimetry' automated cloud-tracking method. *Icarus*, *203*(1), 164–188. https://doi.org/10.1016/j.icarus.2009.05.001

Asay-Davis, X. S., Marcus, P. S., Wong, M. H., & de Pater, I. (2011). Changes in Jupiter's zonal velocity between 1979 and 2008. *Icarus*, *211*(2), 1215–1232. https://doi.org/10.1016/j.icarus.2010.11.018

Banfield, D., Gierasch, P. J., Bell, M., Ustinov, E., Ingersoll, A. P., Vasavada, A. R., et al. (1998). Jupiter's Cloud Structure from Galileo Imaging Data. *Icarus*, *135*(1), 230–250. https://doi.org/10.1006/icar.1998.5985

Bevington, P. R., & Robinson, D. K. (1992). *Data reduction and error analysis for the physical sciences*. McGraw-Hill.

Brueshaber, S. R., & Sayanagi, K. M. (2021). Effects of forcing scale and intensity on the emergence and maintenance of polar vortices on Saturn and Ice Giants. *Icarus*, *361*, 114386. (18pp). https://doi.org/10.1016/j.icarus.2021.114386

Brueshaber, S. R., Sayanagi, K. M., & Dowling, T. E. (2019). Dynamical regimes of giant planet polar vortices. *Icarus*, *323*, 46–61. https://doi.org/10.1016/j.icarus.2019.02.001

Cho, J. Y.-K., de la Torre Juárez, M., Ingersoll, A. P., & Dritschel, D. G. (2001). A high-resolution, three-dimensional model of Jupiter's Great Red Spot. *Journal of Geophysical Research*, *106*(E3), 5099–5106. https://doi.org/10.1029/2000JE001287

Choi, D. S., Banfield, D., Gierasch, P., & Showman, A. P. (2007). Velocity and vorticity measurements of Jupiter's Great Red Spot using automated cloud feature tracking. *Icarus*, *188*(1), 35–46. https://doi.org/10.1016/j.icarus.2006.10.037

Choi, D. S., Showman, A. P., & Vasavada, A. R. (2010). The evolving flow of Jupiter's White Ovals and adjacent cyclones. *Icarus*, *207*(1), 359–372. https://doi.org/10.1016/j.icarus.2009.10.013

de Pater, I., Sault, R. J., Moeckel, C., Moullet, A., Wong, M. H., Goullaud, C., et al. (2019). First ALMA millimeter-wavelength maps of Jupiter, with a multiwavelength study of convection. *The Astronomical Journal*, *158*(4), 139. https://doi.org/10.3847/1538-3881/ab3643

de Pater, I., Wong, M. H., Marcus, P., Luszcz-Cook, S., Ádámkovics, M., Conrad, A., et al. (2010). Persistent rings in and around Jupiter's anticyclones-Observations and theory. *Icarus*, *210*(2), 742–762. https://doi.org/10.1016/j.icarus.2010.07.027

del Río-Gaztelurrutia, T., Sánchez-Lavega, A., Antuñano, A., Legarreta, J., García-Melendo, E., Sayanagi, K. M., et al. (2018). A planetary-scale disturbance in a long living three vortex coupled system in Saturn's atmosphere. *Icarus*, *302*, 499–513. https://doi.org/10.1016/j.icarus.2017.11.029

Dowling, T. E. (1995). Dynamics of Jovian atmospheres. *Annual Review of Fluid Mechanics*, *27*, 293–334. https://doi.org/10.1146/annurev.fl.27.010195.001453

Dowling, T. E., & Ingersoll, A. P. (1988). Potential vorticity and layer thickness variations in the flow around Jupiter's Great Red Spot and White Oval BC. *Journal of the Atmospheric Sciences*, *45*, 1380–1396. https://doi.org/10.1175/1520-0469(1988)045/1380:PVALTV/2.0.CO;2

Dressel, L. (2021). *Wide Field Camera 3 Instrument Handbook, Version 13.0*. Space Telescope Science Institute.

Fletcher, L. N., Orton, G. S., Rogers, J. H., Giles, R. S., Payne, A. V., Irwin, P. G. J., & Vedovato, M. (2017). Moist convection and the 2010–2011 revival of Jupiter's South Equatorial Belt. *Icarus*, *286*, 94–117. https://doi.org/10.1016/j.icarus.2017.01.001

Fletcher, L. N., Orton, G. S., Rogers, J. H., Simon-Miller, A. A., de Pater, I., Wong, M. H., et al. (2011). Jovian temperature and cloud variability during the 2009-2010 fade of the South Equatorial Belt. *Icarus*, *213*(2), 564–580. https://doi.org/10.1016/j.icarus.2011.03.007

Hadland, N., Sankar, R., LeBeau, R. P., & Palotai, C. (2020). EPIC simulations of Neptune's dark spots using an active cloud microphysical model. *Monthly Notices of the Royal Astronomical Society*, *496*(4), 4760–4768. https://doi.org/10.1093/mnras/staa1799

Hassanzadeh, P., Marcus, P. S., & Le Gal, P. (2012). The universal aspect ratio of vortices in rotating stratified flows: Theory and simulation. *Journal of Fluid Mechanics*, *706*, 46–57. https://doi.org/10.1017/jfm.2012.180

Hueso, R., Sánchez-Lavega, A., Rojas, J. F., Simon, A. A., Barry, T., del Río-Gaztelurrutia, T., et al. (2020). Saturn atmospheric dynamics one year after Cassini: Long-lived features and time variations in the drift of the Hexagon. *Icarus*, *336*, 23. https://doi.org/10.1016/j.icarus.2019.113429

LeBeau, R. P., & Dowling, T. E. (1998). EPIC simulations of time-dependent, three-dimensional vortices with application to neptune's great dark spot. *Icarus*, *132*(2), 239–265. https://doi.org/10.1006/icar.1998.5918

Lemasquerier, D., Facchini, G., Favier, B., & Le Bars, M. (2020). Remote determination of the shape of Jupiter's vortices from laboratory experiments. *Nature Physics*, *16*(6), 695–700. https://doi.org/10.1038/s41567-020-0833-9

Magalhães, J. A., Seiff, A., & Young, R. E. (2002). The stratification of Jupiter's troposphere at the Galileo probe entry site. *Icarus*, *158*(2), 410–433. https://doi.org/10.1006/icar.2002.6891

Marcus, P., Asay-Davis, X., Wong, M. H., de Pater, I., & Go, C. (2008). New observations and simulations of Jupiter's Great, Little and Oval Red Spots and Stagnation Points and Their Interactions. *AAS/Division for Planetary Sciences Meeting Abstracts*, *40*. http://ui.adsabs.harvard.edu/abs/2008DPS....40.5303M

Marcus, P. S. (1990). Vortex dynamics in a shearing zonal flow. *Journal of Fluid Mechanics*, *215*, 393–430. https://doi.org/10.1017/S0022112090002695

Marcus, P. S. (2004). Prediction of a global climate change on Jupiter. *Nature*, *428*(6985), 828–831. https://doi.org/10.1038/nature02470

Marcus, P. S., Hassanzadeh, P., Wong, M. H., De Pater, I., Barranco, J., Lee, D. C., & Zhang, A. S. (2019). *On the shedding of Jupiter's Red Flakes. AGU fall meeting abstracts 2019, Abstract P13B-3505*. https://ui.adsabs.harvard.edu/abs/2019AGUFM.P13B3505M

Mitchell, J. L., Beebe, R. F., Ingersoll, A. P., & Garneau, G. W. (1981). Flow fields within Jupiter's Great Red Spot and White Oval BC. *Journal of Geophysical Research*, *86*(A10), 8751–8757. https://doi.org/10.1029/JA086iA10p08751

Moore, D. W., & Saffman, P. G. (1971). Structure of a Line Vortex in an Imposed Strain. In J. H. Olsen, A. Goldburg, & M. Rogers (Eds.), *Aircraft wake turbulence and its detection*. Springer. https://doi.org/10.1007/978-1-4684-8346-8_20

Pedlosky, J. (1987). *Geophysical fluid dynamics* (2nd edition). Springer-Verlag.

Polvani, L. M., Wisdom, J., Dejong, E., & Ingersoll, A. P. (1990). Simple dynamical models of Neptune's great dark spot. *Science*, *249*(4975), 1393–1398. https://doi.org/10.1126/science.249.4975.1393

Press, W. H., Teukolsky, S. A., Vetterling, W. T., & Flannery, B. P. (1992). *Numerical recipes in C. The art of scientific computing*. Cambridge University Press.

Rogers, J., Eichstädt, G., Jacquesson, M., Hansen, C., Orton, G., Momary, T., et al. (2018). The new South Tropical Disturbance and its interaction with the Great Red Spot. European Planetary Science Congress. Abstract EPSC2018-562. https://meetingorganizer.copernicus.org/EPSC2018/EPSC2018-562.pdf

Rogers, J. H. (1995). *The giant planet Jupiter*. Cambridge University Press.

Rogers, J. H. (2018). *Jupiter in 2016–17: Summary of the mid-SEB outbreak*. British Astronomical Association, Jupiter Section Report 17. https://britastro.org/node/8103

Sánchez-Lavega, A., Anguiano-Arteaga, A., Iñurrigarro, P., Garcia-Melendo, E., Legarreta, J., Hueso, R., et al. (2021). Jupiter's Great Red Spot: Strong interactions with incoming anticyclones in 2019. *Journal of Geophysical Research*, *126*(4), 2020JE006686. https://doi.org/10.1029/2020JE006686

Sánchez-Lavega, A., & Gómez, J. M. (1996). The South Equatorial Belt of Jupiter, I: Its life cycle. *Icarus*, *121*(1), 1–17. https://doi.org/10.1006/icar.1996.0067

Sánchez-Lavega, A., Rojas, J. F., & Sada, P. V. (2000). Saturn's zonal winds at cloud level. *Icarus*, *147*(2), 405–420. https://doi.org/10.1006/icar.2000.6449

Sayanagi, K. M., Dyudina, U. A., Ewald, S. P., Fischer, G., Ingersoll, A. P., Kurth, W. S., et al. (2013). Dynamics of Saturn's great storm of 2010-2011 from Cassini ISS and RPWS. *Icarus*, *223*(1), 460–478. https://doi.org/10.1016/j.icarus.2012.12.013

Schultz Tokos, K., & Rossby, T. (1991). Kinematics and Dynamics of a Mediterranean Salt Lens. *Journal of Physical Oceanography*, *21*(6), 879–892. https://doi.org/10.1175/1520-0485(1991)021<0879:KADOAM>2.0.CO;2

Shetty, S., Asay-Davis, X. S., & Marcus, P. S. (2007). On the Interaction of Jupiter's great red spot and zonal jet streams. *Journal of the Atmospheric Sciences*, *64*(12), 4432–4444. https://doi.org/10.1175/2007JAS2097.1

Shetty, S., & Marcus, P. S. (2010). Changes in Jupiter's Great Red Spot (1979-2006) and Oval BA (2000-2006). *Icarus*, *210*(1), 182–201. https://doi.org/10.1016/j.icarus.2010.06.026

Simon, A. A. (2015). Outer Planet Atmospheres Legacy ("OPAL"). *Barbara A. Mikulski Archive for Space Telescopes*, Dataset. https://doi.org/10.17909/T9G593

Simon, A. A., Tabataba-Vakili, F., Cosentino, R., Beebe, R. F., Wong, M. H., & Orton, G. S. (2018). Historical and contemporary trends in the size, drift, and color of Jupiter's Great Red Spot. *The Astronomical Journal*, *155*(4), 151. https://doi.org/10.3847/1538-3881/aaae01

Simon, A. A., Wong, M. H., & Orton, G. S. (2015). First results from the Hubble OPAL Program: Jupiter in 2015. *The Astrophysical Journal*, *812*(1), 55. https://doi.org/10.1088/0004-637X/812/1/55

Simon, A. A., Wong, M. H., Rogers, J. H., Orton, G. S., de Pater, I., Asay-Davis, X., et al. (2014). Dramatic change in Jupiter's Great Red spot from spacecraft observations. *The Astrophysical Journal*, *797*(2), L31. https://doi.org/10.1088/2041-8205/797/2/L31

Smith, B. A., Soderblom, L. A., Banfield, D., Barnet, C., Bailevsky, A. T., Beebe, R. F., et al. (1989). Voyager 2 at Neptune: Imaging science results. *Science*, *246*(4936), 1422–1449. https://doi.org/10.1126/science.246.4936.1422

Sromovsky, L. A., Fry, P. M., & Baines, K. H. (2002). The unusual dynamics of Northern Dark Spots on Neptune. *Icarus*, *156*(1), 16–36. https://doi.org/10.1006/icar.2001.6761

Sromovsky, L. A., Limaye, S. S., & Fry, P. M. (1993). Dynamics of Neptune's Major Cloud Features. *Icarus*, *105*(1), 110–141. https://doi.org/10.1006/icar.1993.1114

Sugiyama, K.-I., Odaka, M., Kuramoto, K., & Hayashi, Y.-Y. (2006). Static stability of the Jovian atmospheres estimated from moist adiabatic profiles. *Geophysical Research Letters*, *33*(3), L03201. https://doi.org/10.1029/2005GL024554

Sun, B., Liu, C., & Wang, F. (2018). Global meridional eddy heat transport inferred from Argo and altimetry observations. *Scientific Reports*, *9*, 1345. https://doi.org/10.1038/s41598-018-38069-2

Sutyrin, G. G. (2020). How Baroclinic vortices intensify resulting from erosion of their cores and/or changing environment. *Ocean Modelling*, *156*, 101711. https://doi.org/10.1016/j.ocemod.2020.101711

Tollefson, J., Wong, M. H., de Pater, I., Simon, A. A., Orton, G. S., Rogers, J. H., et al. (2017). Changes in Jupiter's zonal wind profile preceding and during the Juno mission. *Icarus*, *296*, 163–178. https://doi.org/10.1016/j.icarus.2017.06.007

Trigo-Rodriguez, J. M., Sánchez-Lavega, A., Gómez, J. M., Lecacheux, J., Colas, F., & Miyazaki, I. (2000). The 90-day oscillations of Jupiter's Great Red Spot revisited. *Planetary and Space Science*, *48*(4), 331–339. https://doi.org/10.1016/S0032-0633(00)00002-7

Vasavada, A. R., Ingersoll, A. P., Banfield, D., Bell, M., Gierasch, P. J., Belton, M. J. S., et al. (1998). Galileo imaging of Jupiter's atmosphere: The Great Red Spot, Equatorial Region, and White Ovals. *Icarus*, *135*(1), 265–275. https://doi.org/10.1006/icar.1998.5984

Wong, M. H. (2009). Comment on "Transport of nonmethane hydrocarbons to Jupiter's troposphere by descent of smog particles" by Donald M. Hunten [Icarus 194 (2008) 616 622]. *Icarus*, *199*(1), 231–235. https://doi.org/10.1016/j.icarus.2008.08.017

Wong, M. H. (2021). Jupiter Great Red Spot Velocity Fields from HST/WFC3 (GRSWFC3). *Barbara A. Mikulski Archive for Space Telescopes*, Dataset. https://doi.org/10.17909/t9-jfs3-p240

Wong, M. H., de Pater, I., Asay-Davis, X., Marcus, P. S., & Go, C. Y. (2011). Vertical structure of Jupiter's Oval BA before and after it reddened: What changed? *Icarus*, *215*(1), 211–225. https://doi.org/10.1016/j.icarus.2011.06.032

Wong, M. H., Simon, A. A., Tollefson, J. W., de Pater, I., Barnett, M. N., Hsu, A. I., et al. (2020). High-resolution UV/Optical/IR Imaging of Jupiter in 2016-2019. *The Astrophysical Journal Supplement Series*, *247*(2), 58. https://doi.org/10.3847/1538-4365/ab775f

Yim, E., Billant, P., & Ménesguen, C. (2016). Stability of an isolated pancake vortex in continuously stratified-rotating fluids. *Journal of Fluid Mechanics*, *801*, 508–553. https://doi.org/10.1017/jfm.2016.402

References From the Supporting Information

Iñurrigarro, P., Hueso, R., Legarreta, J., Sánchez-Lavega, A., Eichstädt, G., Rogers, J. H., et al. (2020). Observations and numerical modelling of a convective disturbance in a large-scale cyclone in Jupiter's South Temperate Belt. *Icarus*, *336*, 113475. https://doi.org/10.1016/j.icarus.2019.113475

Karalidi, T., Apai, D., Schneider, G., Hanson, J. R., & Pasachoff, J. M. (2015). Aeolus: A Markov Chain Monte Carlo Code for Mapping Ultracool Atmospheres. An Application on Jupiter and Brown Dwarf HST Light Curves. *The Astrophysical Journal*, *814*(1), 65. https://doi.org/10.1088/0004-637X/814/1/65

Li, C., Ingersoll, A., Klipfel, A., & Brettle, H. (2020). Modeling the stability of polygonal patterns of vortices at the poles of Jupiter as revealed by the Juno spacecraft. *Proceedings of the National Academy of Sciences*, *117*(39), 24082–24087. https://doi.org/10.1073/pnas.2008440117

Orton, G. S., Tabataba-Vakili, F., Eichstädt, G., Rogers, J., Hansen, C. J., Momary, T. W., et al. (2020). A Survey of small-scale waves and wave-like phenomena in Jupiter's atmosphere detected by JunoCam. *Journal of Geophysical Research: Planets*, *125*(7), e06369. https://doi.org/10.1029/2019JE006369

Showman, A. P. (2007). Numerical Simulations of forced shallow-water turbulence: Effects of moist convection on the large-scale circulation of Jupiter and Saturn. *Journal of the Atmospheric Sciences*, *64*(9), 3132. https://doi.org/10.1175/JAS4007.1

Valcke, S., & Verron, J. (1997). Interactions of Baroclinic isolated vortices: The dominant effect of shielding. *Journal of Physical Oceanography*, *27*(4), 524–541. https://doi.org/10.1175/1520-0485(1997)027<0524:IOBIVT>2.0.CO;2

Wong, M. H. (2020). Velocity Field of Jupiter's Great Red Spot in December 2016. *Dryad*, Dataset. https://doi.org/10.6078/D18Q4H